



Aalborg Universitet

AALBORG UNIVERSITY
DENMARK

Common-Ground-Type Single-Source High Step-Up Cascaded Multilevel Inverter for Transformerless PV Applications

Jahan, Hossein Khoun; Kurdkandi, Naser Vosoughi; Abapour, Mehdi; Zare, Kazem; Hosseini, Seyed Hossein; Yang, Y.; Blaabjerg, Frede

Published in:
Mathematics

Creative Commons License
CC BY 4.0

Publication date:
2020

Document Version
Accepted author manuscript, peer reviewed version

[Link to publication from Aalborg University](#)

Citation for published version (APA):

Jahan, H. K., Kurdkandi, N. V., Abapour, M., Zare, K., Hosseini, S. H., Yang, Y., & Blaabjerg, F. (2020). Common-Ground-Type Single-Source High Step-Up Cascaded Multilevel Inverter for Transformerless PV Applications. *Mathematics*, 8(10), 1-17.

General rights

Copyright and moral rights for the publications made accessible in the public portal are retained by the authors and/or other copyright owners and it is a condition of accessing publications that users recognise and abide by the legal requirements associated with these rights.

- ? Users may download and print one copy of any publication from the public portal for the purpose of private study or research.
- ? You may not further distribute the material or use it for any profit-making activity or commercial gain
- ? You may freely distribute the URL identifying the publication in the public portal ?

Take down policy

If you believe that this document breaches copyright please contact us at vbn@aub.aau.dk providing details, and we will remove access to the work immediately and investigate your claim.

1 Article

2 Common-Ground-Type Single-Source High Step-Up 3 Cascaded Multilevel Inverter for Transformerless PV 4 Applications

5 Hossein Khoun Jahan^{1,*}, Naser Vosoughi Kurdkandi¹, Mehdi Abapour¹, Kazem Zare¹, Seyed
6 Hossein Hosseini¹, Yongheng Yang², and Frede Blaabjerg^{2,*}

7 ¹ Faculty of Electrical and Computer Engineering, University of Tabriz; Tabriz, Iran,
8 hosseinkhounjahan@yahoo.com (H.K); naser.vosoughi@yahoo.com (N.V); abapour@tabrizu.ac.ir (M.A);
9 kazem.zare@tabrizu.ac.ir (K.Z); hosseini@tabrizu.ac.ir (S.H.H).

10 ² Department of Energy Technology, Aalborg University, 9220 Aalborg, Denmark; yoy@et.aau.dk (Y.Y);
11 fbl@et.aau (F.B).

12 * Correspondence: hosseinkhounjahan@yahoo.com;

13 Received: date; Accepted: date; Published: date

14 **Abstract:** Cascaded multilevel inverter (CMI) is one type of common inverters in industrial
15 applications. This type of inverter can be synthesized either as a symmetric configuration with
16 several identical H-bridge (HB) cells or as an asymmetric configuration with non-identical HB cells.
17 In PV applications with the CMI, the PV modules can be used to replace the isolated dc sources;
18 however, this brings inter-module leakage currents. To tackle the issue, the single-source CMI is
19 preferred. Furthermore, in a grid-tied PV system, the main constraint is the capacitive leakage
20 current. This problem can be addressed by providing a common ground, which is shared by PV
21 modules and the ac grid. This paper thus proposes a topology that fulfills the mentioned
22 requirements and thus it is a promising inverter in wide industrial area such as PV applications.
23 The proposed CMI topology also features high boosting capability, fault current limiting, and
24 transformerless configuration. To demonstrate the capabilities of this CMI, simulations and
25 experimental results are provided.

26 **Keywords:** Cascaded multilevel inverter; Photovoltaic; Leakage current;

27 1. Introduction

28 Multilevel inverters (MIs) are attractive devices in many industrial applications. These devices
29 can reduce the Total Harmonic Distortion (THD), Electromagnetic interference (EMI), dv/dt ,
30 switching frequency and voltage stress. One of the most regarded applications of MIs is PV
31 application. The neutral point clamped converter (NPC) and CMI are two types of multilevel
32 inverters, which are popular in PV applications [1-2]. Between the two topologies, the CMI stands
33 out for its modularity and high magnitude of the output voltage. However, this topology requires
34 several isolated dc sources. This drawback not only calls for a complex control system, but also it
35 gives rise to inter module leakage currents in grid-tied PV applications. The inter-module leakage
36 currents are resulted from differential-mode voltage (DMV) and common mode voltage CMV
37 variations. In order to tackle the issue, several topologies are suggested in the literature [3-5]. One
38 solution is using only one dc-source along with some passive components. Single-source CMIs are
39 categorized into three types. *i*) Topologies which use low frequency transformers instead of several
40 isolated dc sources. These topologies are referred to as cascaded transformers multilevel inverters
41 (CTMIs) [6-9]. *ii*) Topologies which provide the isolated dc sources by adopting a high-frequency
42 link and a single dc-source (HFLMI) [10, 11]. *iii*) Switched-capacitor (SC) based cascaded multilevel
43 inverter (SC-CMI) [12-13]. The main advantage of CTMIs is their ability to provide galvanic isolation
44 between the dc source and the load/grid. This is also the case when applying HFLMIs in PV

45 applications, where the leakage current issue is addressed. On the contrary, CTMIs need several
46 bulky and inefficient transformers. Although the transformer size in HFLMIs is reduced due to the
47 use of a high frequency link, many rectifiers are required to convert the isolated high frequency
48 voltages to the desired dc voltages. Thus, the reliability decreases and the cost increase in this
49 topology. Alternatively, SC-CMIs employ several capacitors instead of the isolated dc sources.
50 Therefore, the SC-CMI topologies have a compact size and lower cost. However, these kinds of
51 multilevel inverters lack galvanic isolation.

52 Moreover, many attempts have been made to use isolated PV arrays as the isolated dc sources
53 in grid-tied CMIs [14]. However, as illustrated in [15], the main constraint of these configurations is
54 the capacitive leakage currents between the HB cells and grid. Even using an interfacing transformer
55 cannot address the mentioned problem, because inter-module leakage currents appear and circulate
56 between the cascaded HB cells. In [15], the mentioned problem was addressed by equipping each
57 HB cell with additional ac and dc side filters. Apart from limiting various leakage currents, these
58 filters are deemed to eliminate the EMI; however, equipping each cell with several filters increases
59 the volume and cost of the inverter. In [16], several level-double networks (LDN) are used as the
60 auxiliary blocks to enhance the quality of the output voltage. This topology can also offer a common
61 ground between the PV module and the grid, which results in the elimination of the leakage current.
62 Although the suggested topology can eliminate the leakage current in PV applications, balancing of
63 the capacitor voltage in the auxiliary cell is challenging. In another attempt, a two-stage inverter was
64 suggested in [17], which can be regarded as a combination of the H5 and HERIC topologies. When
65 the output voltage is higher than the grid voltage, the inverter operates in the H5 mode; when the dc
66 link voltage decreases, the inverter is switched to the two-stage HERIC mode. This inverter can
67 properly deal with voltage variation. However, it uses a complicated structure and control
68 approach. Moreover a charge pump circuit was employed to eliminate the leakage in [18]. The
69 topology is simple and compact, but it imposes a non-continuous current to the input side. Notably,
70 in [19] a comprehensive study was conducted to investigate the state-of-the-art inverters for
71 grid-tied PV applications.

72 In light of the above, a single-source asymmetric CMI is proposed in this paper, which provides
73 a common ground for ac and dc sides. This topology uses capacitors instead of the isolated dc
74 sources in the HB cells. Each capacitor is independently charged through a charging switch. Since
75 there is a common ground for ac and dc sides, the common mode voltage is zero; hence, this
76 topology can totally eliminate the leakage current in grid-tied PV applications. Another merit of the
77 proposed topology is the capability to boost the input dc voltage; this is also an advantage in many
78 applications such as grid-tied transformerless PV and fuel cell systems. In addition to the mentioned
79 features, the three-phase configuration of the proposed topology draws a continuous input current,
80 which makes it feasible in battery, un-interruptible power supply, and PV applications. The
81 proposed topology can exchange reactive power with the load and the grid as well. Furthermore, it
82 can smoothly charge the capacitors, facilitate the protection, and avoid bulky and expensive
83 transformers in the grid-tied mode. As mentioned, the main issue of the conventional CMI in PV
84 applications is the inter-module leakage currents. However, the proposed topology can address this
85 problem properly and effectively. Compared to the transformer-based single-source multilevel
86 inverters, the proposed topology is smaller in size, lower in cost, and higher in efficiency.
87 Additionally, considering that the SC-based single-source MIs mostly suffer from inrush currents,
88 the proposed topology is however, an inrush-current free CMI, being a promising converter in many
89 industrial applications.

90 The rest of the paper is organized as follows: In section 2, the structure and operation principle
91 of the proposed topology are illustrated. In Section 3, the proposed MI is compared with
92 state-of-the-art MI topology. In section 4 the performance of the proposed topology in off-grid and
93 grid-tied modes is investigated through simulations. Experimental tests are provided in Section 5,
94 where a fifteen-level 0.55 kVA prototype is adopted to demonstrate the off-grid performance of the
95 proposed topology. Moreover, a seven-level 1.5 kVA prototype is used to extract the grid-tied
96 results. Finally, the overall work is concluded in Section 6.

97 **2. Proposed Topology and Operation Principle**

98 **2.1. Conventional CMI in PV Systems**

99 Many solutions are presented in the literature to improve the performance of the CMIs in PV
 100 systems. The main problem arises due to the parasitic capacitor in each HB cell that brings
 101 inter-module leakage currents [20-21]. **These circulating currents cause power loss, EMI, and safety**
 102 **problems [15].** Figures 1(a) and (b) show a grid-tied PV system with a three-cell CMI, and equivalent
 103 circuit of the CMV, DMV and leakage currents, respectively.

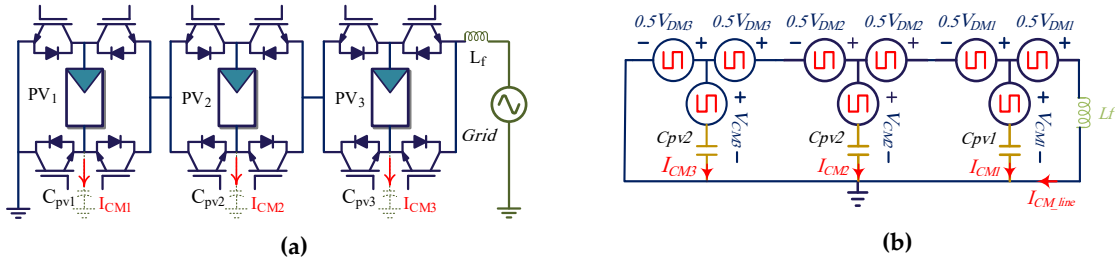


Figure 1. Conventional CMI-based PV system: (a) a three-cell grid-tied CMI; (b) equivalent circuit to illustrate the CMV, DMV and inter-module currents.

104 **2.2. General Structure of the Proposed Topology**

105 The proposed topology is synthesized with two parts, namely the main and charging parts. The
 106 main part is the conventional asymmetric CMI, in which the isolated dc sources are replaced with
 107 capacitors (C_1, C_2, \dots, C_n). The charging part is composed of a single dc source (e.g. a PV string,
 108 fuel-cell, and batteries), a charging inductor, a freewheeling diode and charging switches ($S_{c1}, S_{c2}, \dots,$
 109 S_{cn}). The general grid-tied configuration of the proposed topology (a configuration with n HB cells) is
 110 depicted in figure 2. Where the main part is colored in black, the charging part is in blue.

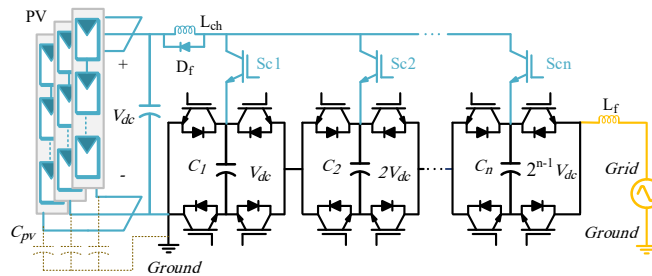


Figure 2. General configuration of the proposed topology in grid-tied PV applications.

111 As mentioned, the most undesirable phenomenon in an SC-based converter is the inrush
 112 currents that emerge in the charging stage of the capacitors. This phenomenon can adversely affect
 113 the charging switches and capacitors. In order to limit these currents, a charging inductor (L_{ch}) is
 114 connected in series with the dc source, as shown in figure 2. This inductor can effectively limit the
 115 inrush currents. On the contrary, the mentioned inductor can cause voltage spikes and commutation
 116 problems in the charging switches. To avoid this and alleviate the EMI, the size of the charging
 117 inductor (L_{ch}) can be obtained as

$$L_{ch} = \frac{1}{(4\pi f)^2 C_n} \tag{1}$$

118 where f and C_n are the output voltage frequency and equivalent capacitance of the capacitors.

119 It should be noted that a larger inductor can be used to further reduce the inrush currents.
 120 However, it can increase the cost and volume of the inverter. A large inductor can also cause
 121 overvoltage across the capacitors. To avoid this, as shown in figure 2, a freewheeling diode (D_f) is
 122 connected in parallel with the inductor.

123 In order to illustrate the operation principle of the proposed topology, a fifteen-level
 124 configuration, which is depicted in figure 3, is exemplified. Table 1 shows the switching pattern for
 125

126 each level and different states of the capacitors. It should be mentioned that in table 1, “on” and “off”
 127 states of the switches are indicated by “1” and “0”. The capacitors in the proposed topology
 128 experience three states namely the charging, discharging, and floating states. In table 1, “C”, “D”,
 129 and “F” denote the charging, discharging, and floating states of the capacitors. In addition, since the
 130 upper switches of the main part (S_{11} , S_{31} , S_{12} , S_{32} , S_{13} , and S_{33}) have complementary states with the
 131 lower switches (S_{21} , S_{41} , S_{22} , S_{42} , S_{23} , and S_{43}), only the states of the upper switches are indicated in table
 132 1 for simplicity.

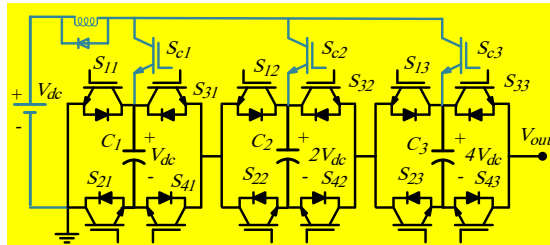


Figure 3. A fifteen-level configuration of the proposed topology.

133 To clarify, the equivalent circuits of the voltage levels are provided. Due to the page limit, only
 134 the positive voltage levels are demonstrated in figure 4. The negative levels can be found referring to
 135 table 1. In figure 4, the charging paths, the capacitors under charge and the load current paths are in
 136 red, blue, and dark blue, respectively.

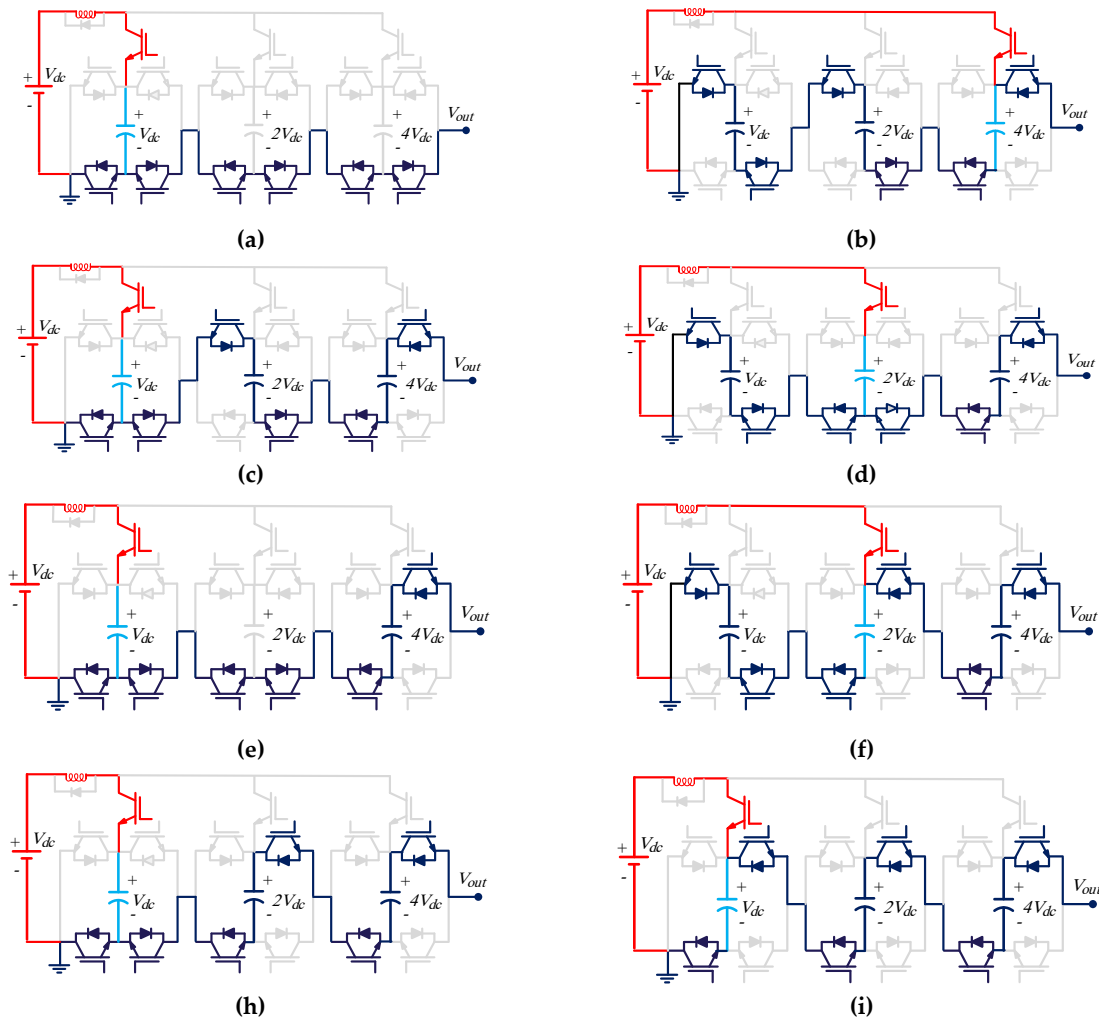


Figure 4. Charging and load current paths: (a) to (h) zero to seventh voltage-levels of the topology in figure 3, respectively, where the PV module is replaced with a dc source for clarity.

137

Table 1. Operation states of components shown in figure 6.

Levels	Main switches	Charging switches	Capacitors	V_{out}
	S_{11}, S_{31}, S_{12}	S_{c1}, S_{c2}, S_{c2}	C_1, C_2, C_3	
	S_{32}, S_{13}, S_{33}			
7	010101	100	C,D,D	$7V_{dc}$
6	000101	100	C,D,D	$6V_{dc}$
5	100101	010	D,C,D	$5V_{dc}$
4	000001	100	C,D,D	$4V_{dc}$
3	100001	010	D,C,D	$3V_{dc}$
2	001001	100	C,D,D	$2V_{dc}$
1	101001	001	D,DC	$1V_{dc}$
0	000000	100	C,F,F	0
-1	100000	010	D,C,D	$-1V_{dc}$
-2	001000	100	C,D,D	$-2V_{dc}$
-3	101000	001	D,D,C	$-3V_{dc}$
-4	000010	100	C,F,D	$-4V_{dc}$
-5	100010	010	D,C,D	$-5V_{dc}$
-6	001010	100	C,D,D	$-6V_{dc}$
-7	101010	000	D,D,D	$-7V_{dc}$

138

139

2.3. Three-Phase Configuration

140

141

142

143

144

145

146

147

148

149

150

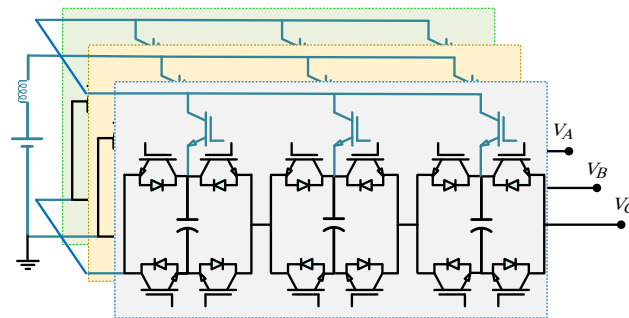
151

152

153

Continuity of the input current in many applications is of high importance. A continuous input current can facilitate the maximum power point tracking (MPPT) process in PV applications and prolong battery life span in storage systems. Referring to table 1, it can be seen that a single-phase configuration of the proposed topology cannot guarantee a continuous input current because there is no possibility to connect the dc source to any of the capacitors when realizing the highest negative voltage level (this is the case for a configuration with any number of voltage-levels). Since the input current is only interrupted in the highest negative voltage level, which is a short interval, this problem will not exist in a three-phase configuration. In such a configuration, when the input current is interrupted in one phase, there are always two paths in the other two phases for the current to flow. Figure 5 depicts the general three-phase configuration of the proposed topology. It is worth mentioning that in the three-phase configuration, the CMV is reduced but not totally eliminated. Thus in a grid-tied PV application with the three-phase configuration, a limited leakage current is achieved. However, the inter-module leakage currents are totally cancelled out in this configuration.

154



155

Figure 5. General three-phase configuration of the proposed topology.

156

2.4. Component design

157

158

Referring to figure 4 and table 1, it is seen that during one cycle, the lower the dc voltage an HB cell contains, the longer time it resides in the charging mode. For example, as shown in table 1, the

159 first HB cell, which contains 1 pu voltage, resides in the charging mode for eight times. The number
 160 of being in the charging mode for the second and third HB cells is four and two, respectively. Thus,
 161 in an l -level structure, the number of being in the charging state for the n^{th} HB cell is calculated as

$$162 \quad Nch_n = 2^{\frac{\ln(l+1)}{\ln 2} - n} \quad (2)$$

163 In respect to this, an HB cell with a higher dc voltage will provides the load current for a longer
 164 time than others. Therefore, it experiences the highest voltage ripple. The highest voltage ripple of
 165 the n^{th} HB cell (Δv_n) is given as

$$166 \quad \begin{cases} \Delta v_n = \frac{I_m \Delta t_n}{C_n} \\ \Delta t_n = T(l - Nch_n) \end{cases} \quad (3)$$

167 where I_m , T , and C_n are the maximum value of the load current, time duration of a cycle, and
 168 capacitance of the n^{th} capacitor, respectively. This equation can be used to select a proper capacitor
 169 for the n^{th} HB cell.

170 Considering Fig. 2, the equivalent circuit of the capacitor experiencing the highest voltage
 171 ripple (C_n) is shown in Fig. 6. Taking the parameters indicated in Fig. 6 into account, the
 172 instantaneous voltage in the n^{th} capacitor and the voltage of the mentioned capacitor at the end of a
 173 half cycle are, respectively given as

$$174 \quad v_{c_n}(t) = (2^{n-1})v_{dc} \frac{-t}{RC_n} \quad (4)$$

$$175 \quad v_{c_n}(T_d) = (2^{n-1})v_{dc} \frac{-T_d}{RC_n} \quad (5)$$

176 The maximum voltage ripple in the n^{th} capacitor can be given as

$$177 \quad \Delta v_{c_n} = fT_d((2^{n-1})v_{dc} - v_{c_n}(T_d)) = fT_d(2^{n-1})v_{dc}(1 - e^{\frac{-T_d}{RC_n}}) \quad (6)$$

178

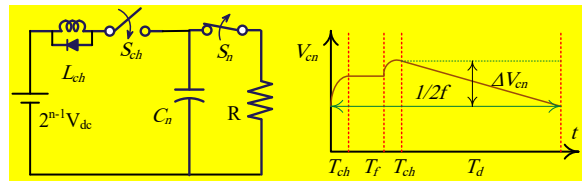


Fig. 6. Equivalent circuit and discharging diagram of a capacitor in an HB cell.

179

180 As it is an asymmetric topology, the HB cells in the proposed topology include different dc
 181 voltage values. Considering v_{dc} as the input voltage, the voltage across the n^{th} cell is given as

$$182 \quad V_{c_n} = 2^{n-1}v_{dc} \quad (7)$$

183 The voltage stress on the main and charging switches in the n^{th} HB cell is equal to the voltage of
 184 capacitor in that HB cell.

185 The peak output voltage of an n -cell configuration is given as

$$186 \quad v_m = v_{dc} \sum_{k=1}^n 2^{k-1} \quad (8)$$

187 The number of switches of an l -level configuration of the proposed and conventional
 188 asymmetric CMI topologies is, respectively, indicated as

$$189 \quad N_{sw}^P = \frac{5 \ln(\frac{l+1}{2})}{\ln 2} \quad (9)$$

$$190 \quad N_{sw}^C = \frac{4 \ln(\frac{l+1}{2})}{\ln 2} \quad (10)$$

191 This implies that the proposed topology requires one extra switch in each cell (one charging
 192 switch for each cell).

193 The total voltage stresses of the switches in the proposed and the conventional asymmetric CMI
 194 topologies are, respectively, indicated as

$$195 \quad TVS_p = \frac{5v_{dc}}{N_{sw}^P} \sum_{k=1}^{N_{sw}^P/5} 2^{k-1} \quad (11)$$

$$196 \quad TVS_c = \frac{4v_{dc}}{N_{sw}^C} \sum_{k=1}^{N_{sw}^C/4} 2^{k-1} \quad (12)$$

197 Implying that the voltage stresses of the switches in both topologies are the same.

198 **3. Benchmarking With Prior-Art Inverters**

199 Several efforts have been done to make the CMI compatible with grid-tied PV applications. The
 200 main difficulties with the CMI in PV applications are the leakage current and complicated MPPT
 201 [14]. Single-source CMIs facilitate the MPPT, but the leakage current problem remains. A
 202 transformer can solve the problem, however, transformers are not recommended in grid-tied PV
 203 applications due to extra power losses and additional costs. Therefore, as stated previously the
 204 SC-based CMI can fulfill many requirements. The state-of-the-art PV MI topologies are compared
 205 with the proposed MI topology in this section to assess its pros and cons. Table 2 lists the main
 206 features of the considered MI topologies.

207 In table, N_{sw} , N_d , N_c , G , and TSV are the number of switches, diodes, capacitors, voltage gain, and
 208 the total voltage standing of the switches. The TSV is calculated as

209
$$TSV = \frac{\sum_{n=0}^{n=k} V_{swn} + \sum_{n=0}^{n=k} V_{sdn}}{V_{out}} \quad (12)$$

Table 2. Comparison

Topology	N_{sw}	N_d	N_c	G	TSV	Coupled inductor	Leakage current limiting
[22]	14	0	2	3	4.67	no	no
[23]	12	-	2	2	5.5	no	no
[24]	10	-	2	0.5	8	yes	yes
[25]	8	3	3	4	5.75	no	no
[26]	12	-	3	4	5.25	no	no
[27]	9	-	2	2	5.5	no	no
[28]	11	-	3	2	5	no	no
[29]	8	4	4	2	6	no	no
[Proposed]	10	0	2	3	5	no	yes

210 The proposed topology and the topology in [29] can be scaled up to obtain higher voltage gains
 211 and levels. However, this is not the case for the other topologies. Since the proposed MI topology is
 212 common-ground-type inverter and the topology in [24] is a mid-point-grounded topology, these two
 213 topologies can limit the leakage current in grid-tied PV applications. In this regard, the other
 214 topologies listed in table 2 encounter serious problems. The main disadvantage of the MI topologies
 215 in [24] and [25] is that they require a complicated control approach to balance the voltages across the
 216 capacitors. The voltage balancing system of these topologies should sense the direction of the ac
 217 current and the capacitor voltage magnitude, and then the sensed values are processed though the
 218 processor to execute the right switching pattern to balance the voltage of the capacitors. However,
 219 this does not happen in the other topologies and the proposed one. Notably, the topology in [23],
 220 [25], [27] and [28] suffer from high inrush currents in the charging stage of the capacitor. Owing to
 221 the controlled voltage balancing of the capacitors, the inrush current does not appear in [31] and [33]
 222 topology. In the proposed topology and the topology in [29], the inrush current is limited through
 223 the charging inductor. As it is seen in table 2, the proposed inverter has fairly low TSV, high voltage
 224 gain and fewer components.

225 **4. Simulation Results**

226 In order to verify the performance of the proposed topology, both the single-phase and
 227 three-phase configurations are simulated under Matlab/Simulink. The main parts in the considered
 228 configurations are assumed to be a fifteen-level CMI. The simulated models are tested under off-grid

229 and grid-tied modes. In the off-grid mode, a general dc source supplies the load through the
 230 proposed topology.

231 4.1. Off-grid mode

232 As illustrated earlier, the three-phase and single-phase configurations only differ in the input
 233 current shapes. For this reason, mostly the single-phase configuration is investigated. Table 3 shows
 234 the characteristics of the utilized components in the off-grid mode. Figure 7(a) shows the output and
 235 capacitor voltages under no-load condition. A Fast Fourier Transform (FFT) analysis of the output
 236 voltage is depicted in figure 7(b).

Table 3. Components of the Off-grid Model.

Component	Value	Component	Value
V_{dc}	46 V	$L_{ch}(3\phi)$	0.5 mH
Power rating	550 W	C_1, C_2, C_3	3300 μF
$L_{ch}(\phi)$	1.8 mH	f_{sw}	5 kHz
Reference voltage	220 V (RMS), 50 Hz		

237

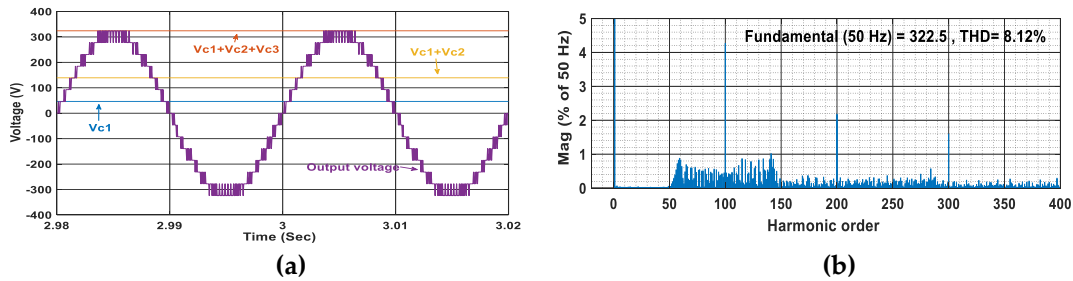


Figure 7. Simulation results of the single-phase configuration in the off-grid mode (no-load condition): (a) capacitor and output voltages; (b) FFT analysis of the output voltage

238 Furthermore, the output voltage, load current, and capacitor voltages, when supplying a purely
 239 resistive load of 0.55 kW, are shown in figure 8(a). As seen in figure 8(a), under this condition, the
 240 voltage across the capacitors is properly balanced through the charging circuit. Additionally, the
 241 capacitor currents along with the input current under the studied loading condition are shown in
 242 figure 8(b). It can be seen that the charging unit can properly limit the inrush current of the
 243 capacitors. However, the main demerit of the charging process is the discontinuity of the input
 244 current due to the absence of a path for the input current when developing the highest negative
 245 voltage level.

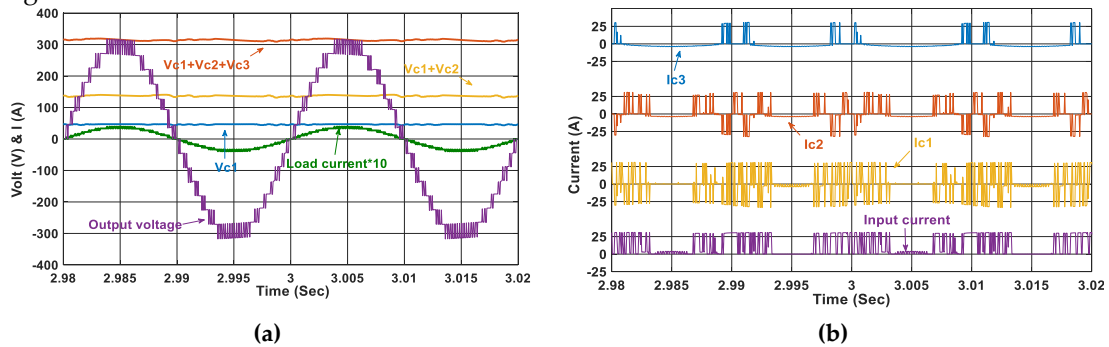


Figure 8. Simulation results of the single-phase configuration in the off-grid mode (under a purely resistive loading condition): (a) load current along with the capacitor and output voltages; (b) capacitor and input currents.

246 In order to demonstrate the ability of the proposed topology to provide reactive power, a
 247 resistive-inductive load of 0.5 kW+0.35 kVar is connected. Figure 9(a) shows the output voltage and
 248 load current under the mentioned condition. As shown in figure 9(a), the proposed topology can
 249 satisfactorily supply the reactive power. Additionally, the voltage stress and current of the charging

250 switches are shown in figure 9(b). According to figure 9(b), it is known that the charging switch in
 251 the last cells can tolerate the highest voltage stress.

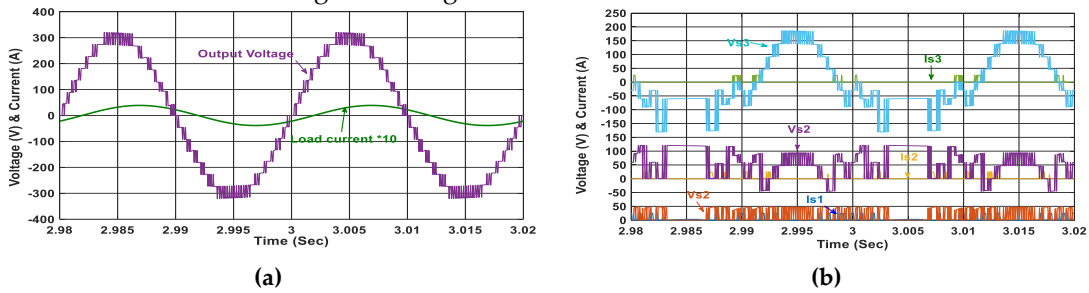


Figure 9. Simulation results of the single-phase configuration in the off-grid mode (under a resistive-inductive loading condition): **(a)** load current and output voltage; **(b)** voltage stress and current of the charging switches.

252 As mentioned previously, a three-phase configuration of the proposed topology draws a
 253 continuous current from the input side. This is proven by considering a three-phase fifteen-level
 254 configuration, which supplies a balanced three-phase load under three loading cases (3.8 kW, 4.8
 255 kW+1.2 kVar, 3 kW+1.2 kVar). The input current of the phases and the total input current under the
 256 mentioned loading condition are shown in figure 10(a). As it is seen in figure 10(a), the input current
 257 is a continuous current. Moreover, the output voltages together with the load current under the
 258 mentioned condition are shown in figure 10(b) and (c), respectively. When the freewheeling diode is
 259 removed, the capacitors are exposed to overvoltage at the initial instance. Soft starting strategies can
 260 be employed to avoid the overvoltage of the capacitors.

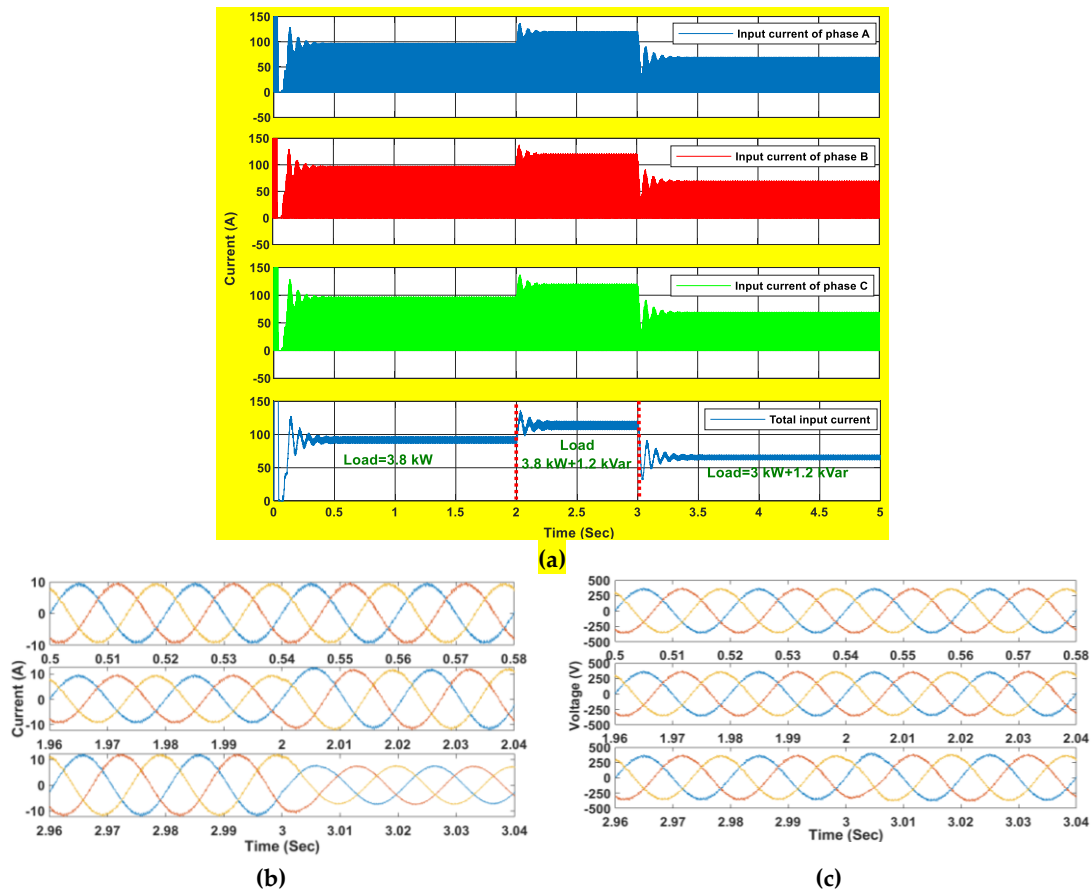


Figure 10. Simulation results of the three-phase configuration in the off-grid mode: **(a)** input current of the phase and total input current; **(b)** load current; **(c)** output voltage.

262 Similar to the off-grid mode, a fifteen-level configuration of the proposed topology is used to
 263 deliver the desired powers to the grid. To this end, the ac components are transferred to the dq0
 264 frame and two proportional-integral (PI) controllers are employed to control the active and reactive
 265 powers. Table 4 shows the characteristics of the considered system.

Table 4. component of the grid-connected model

K_i	42.3	Grid-side filter	2.8 mH + 30 m Ω
K_p	700	f_{sw}	5 kHz
$V_{g_{max}}$	320 V	L_{ch}	1.8 mH
f	50 Hz	C_1, C_2, C_3	3300 μ F

266 The simulation results of the single-phase grid-connected model are shown in figure 11. The
 267 desired (reference) and delivered active power to the grid is shown in figure 11(a). The reference of
 268 the active power can be obtained by the MPPT system in PV applications. The reference and
 269 developed reactive powers are exhibited in figure 11(b). As shown in figure 11(b), the proposed
 270 topology has succeeded to provide a bidirectional reactive power flow. The input current is depicted
 271 in figure 11(c). The output voltage of the inverter along with the injected current is exhibited in
 272 figure 11(d).

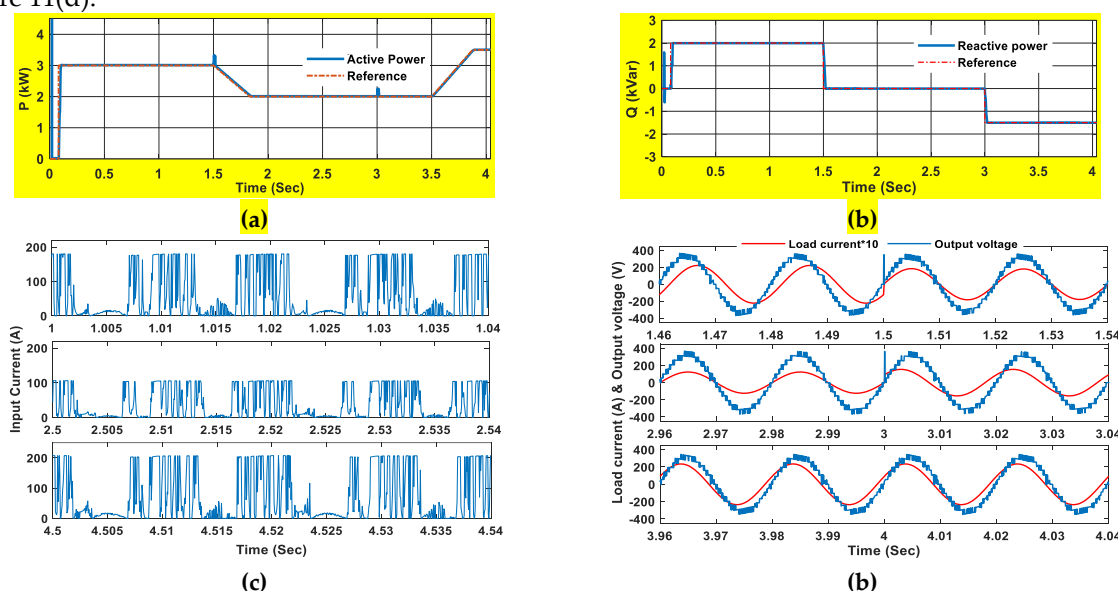


Figure 11. Simulation results of the single-phase grid-connected model: (a) the developed and reference of the active power; (b) the developed and reference of the active power; (c) input current; (d) output voltage and load current.

273 It should be pointed out that one of the significant features of the proposed MI topology is its
 274 ability to eliminate the leakage current in grid-tied PV systems without using any additional
 275 components.

276 Furthermore, the simulation results of a grid-connected three-phase model are demonstrated in
 277 figure 12. The injected active and reactive powers to the grid are depicted in figures 12(a) and (b). As
 278 it is seen in figure 12, the proposed MI has deservedly developed the desired powers.

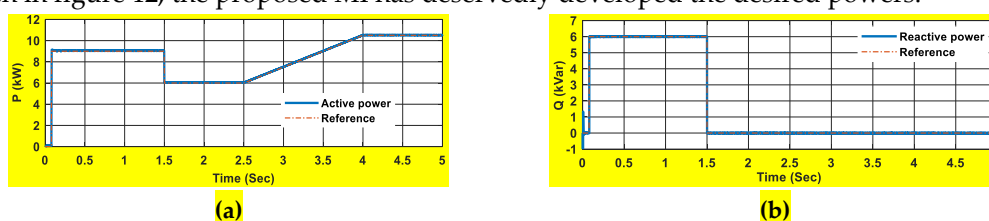


Figure 12. Simulation results of the active and reactive power of the three-phase grid-connected model: (a) the injected active power to the grid; (b) the injected reactive power to the grid.

279 As discussed previously the three-phase configuration of the proposed topology draws a
 280 continuous current from the dc-link. Figure 13(a) shows the input current and proves this. In order
 281 to investigate the leakage current, a parasitic capacitor of 200 nF is considered between the negative
 282 pole of the dc-side and ac-ground, figure 13(b) shows the leakage current. As shown in figure 13(b),
 283 the RMS value of the leakage current is in the acceptable range. However, it is possible to reduce it
 284 through a proper control and/or switching approaches. It is worth mentioning that since the
 285 proposed topology does not use PV modules inside the H-bridge cells, there are no inter-module
 286 leakage currents.

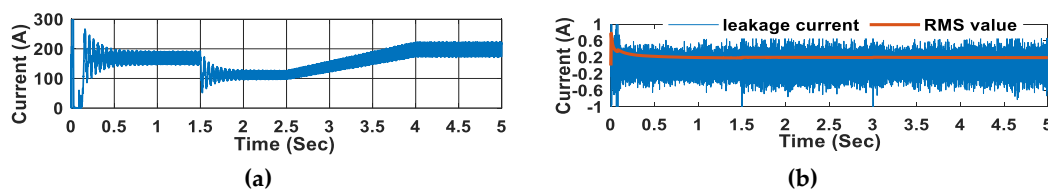


Figure 13. Simulation results of input and leakage current of the three-phase grid-connected model: (a) input current; (b) leakage current.

287 Furthermore the output voltage and the injected current are shown in figure 14. It is to be noted
 288 that this paper is not aimed at designing a proper control system. It is possible to obtain a more
 289 accurate result through a precise control approach.

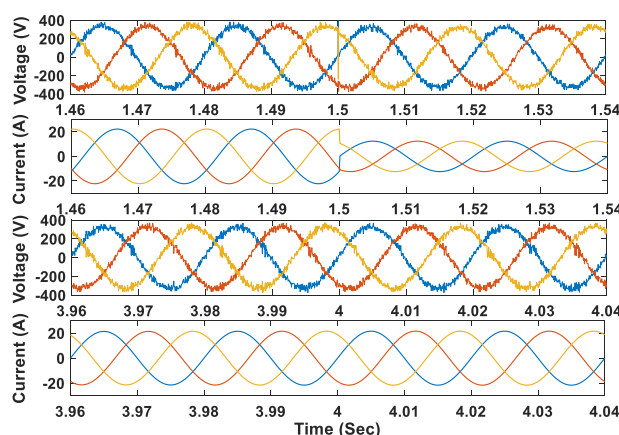


Figure 14. Simulation results of the output voltage and injected current of the three-phase grid-connected model.

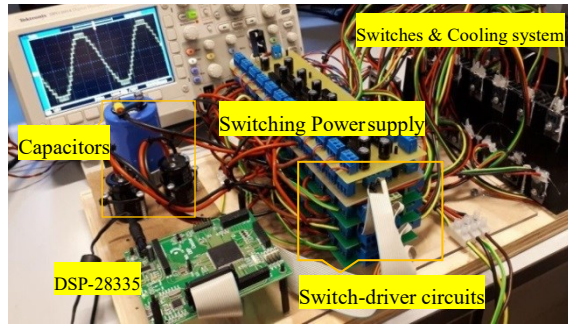
290 **5. Experimental Results**

291 *5.1. Off-grid Results*

292 In order to validate the feasibility of the proposed topology, a laboratory-scale prototype is
 293 tested. Figure 15 depicts the employed prototype and table 5 lists the utilized components. It should
 294 be noted that the level-shifted SPWM strategy is adopted to compute the switching signals.

Table 5. Electrical Parameters and Component Specifications

Component	Specification	Electrical parameter	Value
Main Switches	IRFP350	Resistive load	550 W
Charging switches	IRFP460	RL load	650 VA
Opto-coupler	TLP250	$V_{out}(RMS)$	220 v, 50 Hz
Capacitors	3300 μF	V_{dc}	47 V
L_{ch}	2.8 mH	f_{sw}	5 kHz
Diodes	FFPF20UP40S	# of HB cells	3 (15-level)



296

297

Figure 15. Experimental setup of the proposed topology (15-level).

298

299

300

301

302

Figure 16 exhibits the output voltage under the no-load condition and the FFT analysis of the voltage. As it is seen, the harmonics around the fundamental frequency have negligible magnitude, while the harmonics around the multiples of the switching frequency are of high amplitude. Since these harmonics are far away from the fundamental frequency, they can easily be eliminated using small filters.

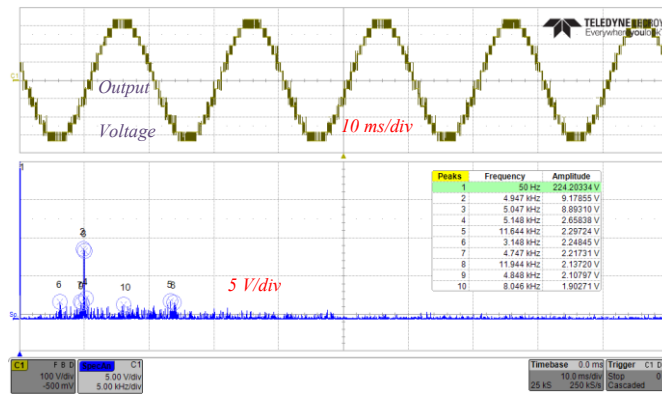


Figure 16. Measured output voltage of the proposed single-phase configuration (15-level) under no-load condition and its FFT analysis.

303

304

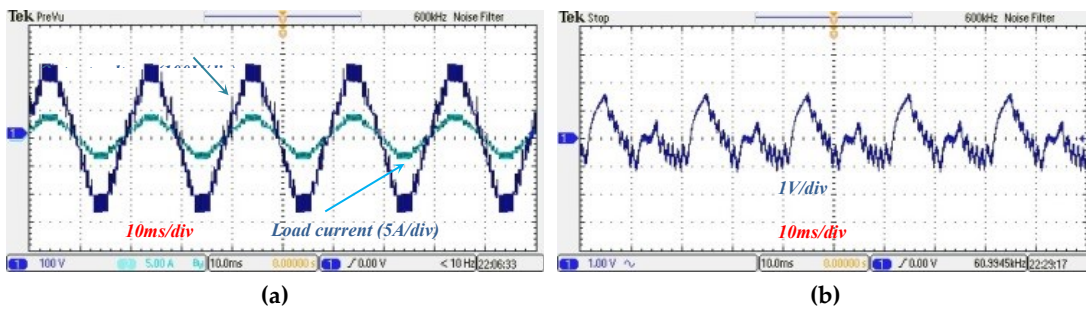
305

306

307

308

The output voltage along with the load current, when the prototype supplies a purely resistive load of 550 W is shown in figure 17(a). In order to assess the voltage ripple of the capacitors, the ac components of the capacitor voltages are shown in figures 17(b), (c) and (d). Additionally, the charging current of the capacitor under 550 W load is shown in figure 17(e). As it is seen, there is no sharp spike on the charging current of the capacitors, which implies that the charging inductor smoothen the charging currents.



(a)

(b)

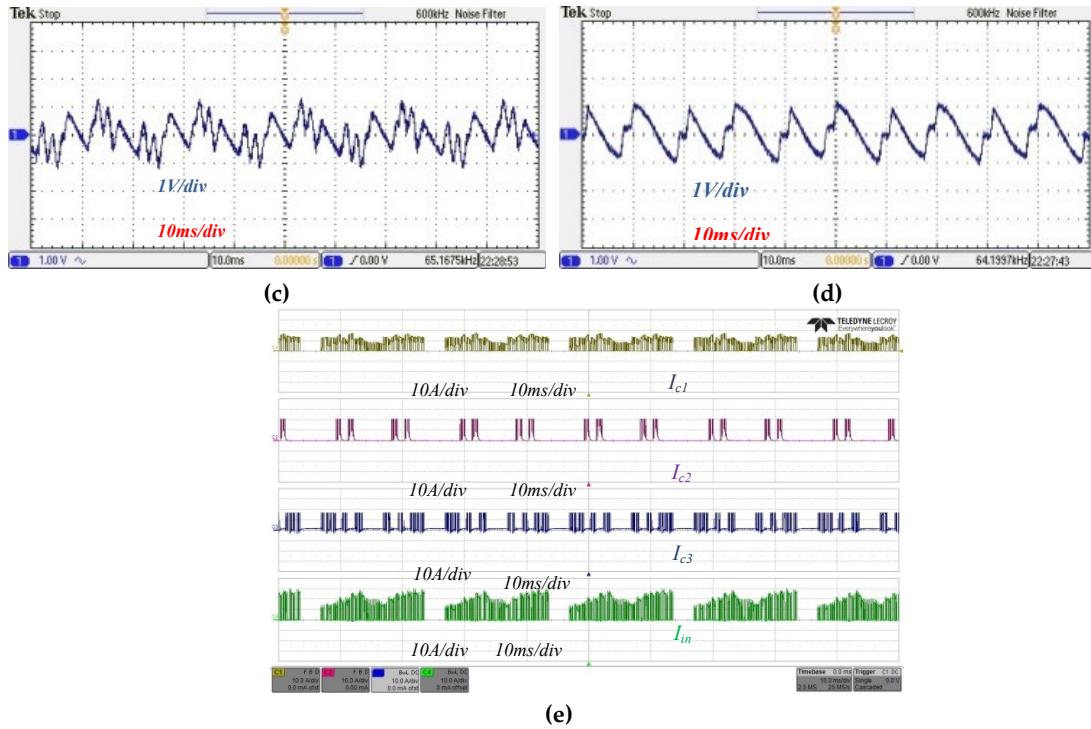


Figure 17. Experimental results under a purely resistive loading condition: (a) output voltage and load current under the purely resistive loading condition; (b), (c), and (d) ac components of the capacitor voltages; (e) input current and charging current of the capacitors.

309 In order to prove the capability of the proposed topology to provide reactive power, a
 310 resistive-inductive load of 500 W+350 Var is then considered. Figure 18 exhibits the output voltage
 311 and load current under this condition. As it can be seen, the proposed topology can supply the
 312 reactive power without any constraints.

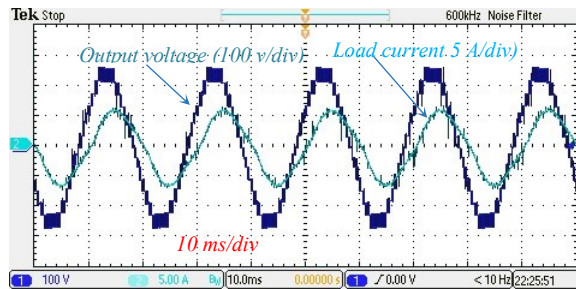


Figure 18. Output voltage and load current under the inductive-resistive loading condition.

5.2. Grid-tied results

315 In order to extract the grid-tied results a seven-level prototype with two cells is employed. The
 316 characteristic of the prototype and grid is listed in table 7. In this test the sample based current
 317 control is used to inject the desired active and reactive powers to the grid.
 318

Table 7. Component Of The Grid-Connected Model.

Main Switches	FQA14N30	Grid-side filter	1.73 mH
Charging switches	STP30NM30N	Switching frequency (f_{sw})	22 kHz
RMS grid voltage	220 V	L_{ch}	1.6 mH
Grid frequency (f)	50 Hz	$C_1, C_2,$	3300 μ F

319 Three scenarios are considered in grid-tied test. In the first scenario a pure active power of 1.5
 320 kW is injected to the grid. The injected current and grid voltage under this condition are shown in

321 figure 19(a). The FFT analysis of the injected current under the mentioned condition is shown in
 322 figure 19(b). Furthermore, the output voltage of the inverter along with the provided current is
 323 shown in figure 19(c).
 324

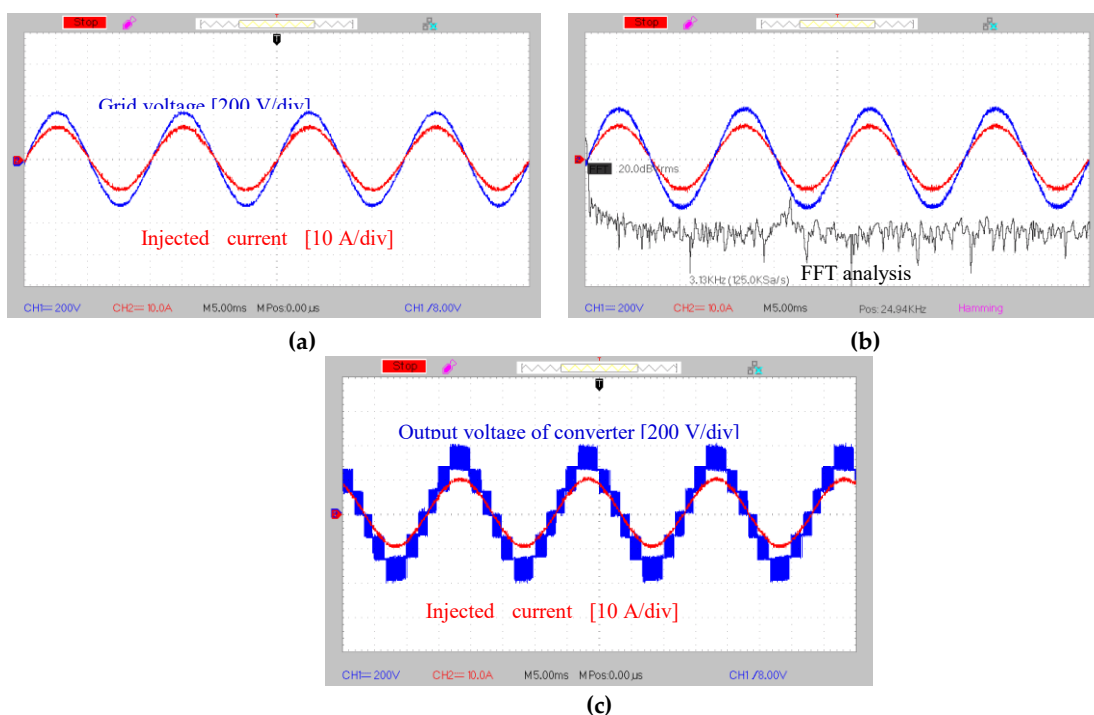


Figure 19. Grid-tied results of the active power: (a) grid voltage and injected current; (b) FFT analysis of the injected current; (c) output voltage and current of the prototype.

325 In the second scenario the active power of 1.2 kW and reactive power of 0.9 kVar is injected to
 326 the grid and in the third scenario the active power of 1.2 kW is injected to the grid and reactive
 327 power of 0.9 kVar absorbed from the grid. The grid voltage together with the injected current to the
 328 grid is shown in figure 20(a) and (b).

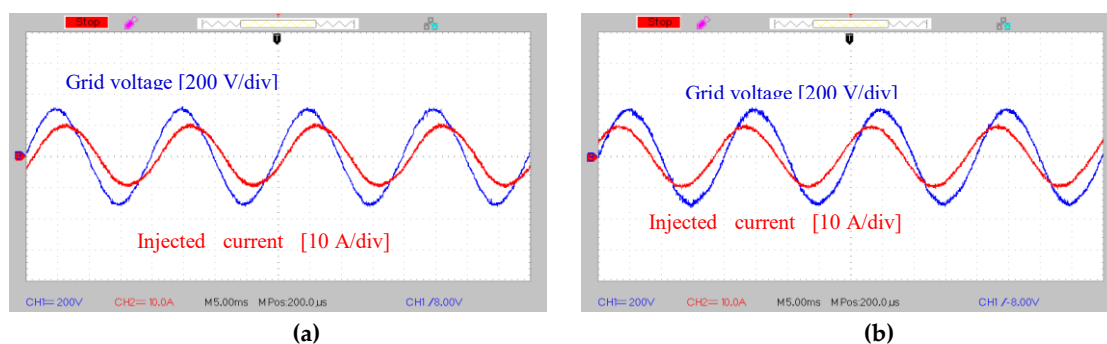


Figure 20. Grid-tied results of the injected current: (a) the output voltage and load current when injecting the active and reactive current to the grid; (b) grid-voltage and injected current when injecting the active power and absorbing the reactive power.

329 The seven-level prototype for grid-tied application is exhibited in figure 21.

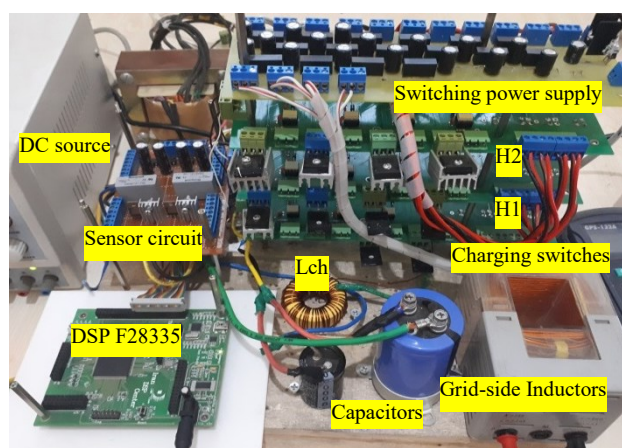


Figure 21. Seven-level setup for grid-tied application.

6. Conclusion

In this paper, a single-source high step-up asymmetric power converter topology was proposed. The proposed topology offers several advantages in many industrial applications such as PV, fuel cell and etc. It is synthesized with two parts, namely the main and charging parts. The main part is the same as the conventional asymmetric CMI with certain capacitors instead of the isolated dc sources. The charging part, however, consists of charging switches, a charging inductor, a freewheeling diode, and one dc source. The main feature of the proposed topology is to provide a common-ground for ac and dc sides, which eliminates the leakage current in grid-tied PV applications. It also has the ability to boost the input voltage. Thus, in the grid-tied PV applications, bulky and expensive transformers can be avoided. Moreover, it uses only one dc source, at the expense of using many switches, employing many switches can be count as the main demerit of the proposed inverter. Simulations and experiments were performed to verify the effectiveness of the proposed topology. Through simulations, the performances of the suggested topology with single- and three-phase configuration in both off-grid and grid-tied conditions were assessed. In the experimental tests, the performance of the proposed topology was studied in the presence of a 550-VA load. Moreover, using a 1.5 kVA seven-level prototype the grid-tied results were provided. Both results have demonstrated the feasibility of the proposed multilevel inverter in terms of the ability to develop a boosted voltage of high quality using only one dc source.

References

- [1] F. Wu; X. Li; F. Feng; and H. B. Gooi. Modified cascaded multilevel grid-connected inverter to enhance European efficiency and several extended topologies, *IEEE Trans. Ind. Inform.*, Dec. 2015, vol. 11, no. 6, pp. 1358 – 1365.
- [2] H. Sepahvand; J. Liao; M. Ferdowsi; and K. A. Corzine. Capacitor voltage regulation in single-DC-source cascaded H-bridge multilevel converters using phase-shift modulation, *IEEE Trans. Ind. Electron.*, Sept. 2013, vol. 60, no. 9, pp. 3619 – 3626.
- [3] M. R. Banaei; H. Khoun Jahan; and E. Salary. Single-source cascaded transformers multilevel inverter with reduced number of switches, *IET Power Electron.*, Nov. 2012, vol. 5, no. 9, pp. 1748 – 1753.
- [4] S. Vazquez; J. I. Leon; L. G. Franquelo; J. J. Padilla; and J. M. Carrasco. DC-voltage-ratio control strategy for multilevel cascaded converters fed with a single DC source, *IEEE Trans. Ind. Electron.*, Jul. 2009, vol. 56, no. 7, pp. 2513 – 2521.
- [5] A. Taghvaie; J. Adabi; and M. Rezanejad. A multilevel inverter structure based on a combination of switched-capacitors and DC sources, *IEEE Trans. Ind. Inform.*, Oct. 2017, vol. 13, no. 5, pp. 2162 – 2171.
- [6] H. Khoun Jahan; K. Zare; and M. Abapour; Verification of a low components nine-level cascaded-transformer multilevel inverter in grid- tied mode, *IEEE J. Emerg. Sele.Topi. Power Electron.*, 2018, vol. 6, no. 1, pp. 429-440,
- [7] S. G. Song; F. Soon Kang; and S. J. Park. Cascaded multilevel inverter employing three-phase transformers and single DC input, *IEEE Trans. Ind. Electron.*, Jun. 2009, vol. 56, no. 6, pp. 2005 – 2014.

- 370 [8] H. Khoun Jahan; M. Naseri, M. M. Haji-Esmaili; M. Abapour, and K. Zare. Low component merged
371 cells cascaded-transformer multilevel inverter featuring an enhanced reliability, *IET Power Electron.*,
372 Jun. 2017, vol. 10, no. 8, pp. 855 – 862.
- 373 [9] A. K. Panda; and Y. Suresh. Performance of cascaded multilevel inverter by employing single and
374 three-phase transformers, *IET Power Electron.*, Nov. 2012, vol. 5, no. 9, pp. 1694 – 1705,
- 375 [10] J. Pereda; and J. Dixon. High-frequency link: A solution for using only one dc source in asymmetric
376 cascaded multilevel inverters, *IEEE Trans. Ind. Electron.*, Sep. 2011, vol. 58, no. 9, pp. 3884 – 3892.
- 377 [11] L. Wang; D. Zhang; Y. Wang; B. Wu; and H. S. Athab. Power and voltage balance control of a novel
378 three-phase solid-state transformer using multilevel cascaded H-bridge inverters for microgrid
379 applications, *IEEE Trans. Power Electron.*, Apr. 2016, vol. 31, no. 4, pp. 3289 – 3301.
- 380 [12] R. Barzegarkhoo; H. M. Kojabadi; E. Zamiry; N. Vosough; and L. Chang. Generalized structure for a
381 single phase switched-capacitor multilevel inverter using a new multiple DC link producer with
382 reduced number of switches, *IEEE Trans. Power Electron.*, Aug. 2016, vol. 31, no. 8, pp. 5604 – 5617.
- 383 [13] Z. Du, B. Ozpineci; L. M. Tolbert; and J. N. Chiasson. DC-AC Cascaded H-bridge multilevel boost
384 inverter with no inductors for electric/hybrid electric vehicle applications, *IEEE Trans. Ind. Appl.*, May
385 2009, vol. 45, no. 3, pp. 963 – 970.
- 386 [14] E. Villanueva; P. Correa, J. Rodriguez; and M. Pacas. Control of a single-phase cascaded H-bridge
387 multilevel inverter for grid-connected photovoltaic systems, *IEEE Trans. Ind. Electron.*, Nov. 2009, vol.
388 56, no. 11, pp. 4399 – 4406.
- 389 [15] Y. Zhou; and H. Li. Analysis and suppression of leakage current in cascaded-multilevel-inverter-based
390 PV systems, *IEEE Trans. Power Electron.*, Oct. 2014, vol. 29, no. 10, pp. 5265 – 5277.
- 391 [16] A. Kadam; and A. Shukla. A multilevel transformerless inverter employing ground connection
392 between PV negative terminal and grid neutral point, *IEEE Trans. Ind. Electron.*, Nov. 2017, vol. 64, no.
393 11, pp. 8897 – 8907.
- 394 [17] Y. P. Siwakoti; F. Blaabjerg. A single-phase transformerless inverter with charge pump circuit concept
395 for grid-tied PV applications, *IEEE Trans. Ind. Electron.*, Mar. 2018, vol. 65, no. 3, pp. 2100 – 2111.
- 396 [18] A. Anurag; N. Deshmukh; A. Maguluri; and S. Anand. Integrated DC-DC Converter Based
397 Grid-Connected Transformerless Photovoltaic Inverter With Extended Input Voltage Range, *IEEE*
398 *Trans. Power Electron.*, Oct. 2018, vol. 33, no. 10, pp. 8322 – 8330.
- 399 [19] M. N. H Khan; Mo. Forouzesh; Y. P Siwakoti; L. Li; T. Kerekes; and F. Blaabjerg. Transformerless
400 Inverter Topologies for Single-Phase Photovoltaic Systems: A Comparative Review, *IEEE J. Emerg.*
401 *Sele.Topi. Power Electron.*, Apr. 2019, vol. 65, no. 2, pp.805 - 835,
- 402 [20] V. V. S. Pradeep Kumar; and B. G. Fernandes. Minimization of inter-module leakage current in
403 cascaded H-bridge multilevel inverters for grid connected solar PV applications, in *Proc. IEEE Appl.*
404 *Power Electron. Conf. Expo.*, Mar. 2016, pp. 2673-2678,
- 405 [21] F. Wang; Z. Li; H. T. Do; and D. Zhang. A modified phase disposition pulse width modulation to
406 suppress the leakage current for the transformerless cascaded H-bridge inverters, *IEEE Trans. Ind.*
407 *Electron.*, Feb. 2018, vol. 65, no. 2, pp. 1281-1289,
- 408 [22] X. Sun; B. Wang; Y. Zhou; W. Wang; H. Du; Z. Lu. A Single DC Source Cascaded Seven-Level Inverter
409 Integrating Switched-Capacitor Techniques, *IEEE Trans. Ind. Electron.*, Nov. 2016, vol. 63, no. 11, pp.
410 7184 - 7194,
- 411 [23] S. S. Lee, "Single-Stage Switched-Capacitor Module (S3CM) Topology for Cascaded Multilevel
412 Inverter," in *IEEE Transactions on Power Electronics*, vol. 33, no. 10, pp. 8204-8207, Oct. 2018, doi:
413 10.1109/TPEL.2018.2805685.
- 414 [24] C. Phanikumar, J. Roy and V. Agarwal, "A Hybrid Nine-Level, 1- ϕ Grid Connected Multilevel Inverter
415 With Low Switch Count and Innovative Voltage Regulation Techniques Across Auxiliary Capacitor,"
416 in *IEEE Transactions on Power Electronics*, vol. 34, no. 3, pp. 2159-2170, March 2019, doi:
417 10.1109/TPEL.2018.2846628.
- 418 [25] J. Liu, W. Lin, J. Wu and J. Zeng, "A Novel Nine-Level Quadruple Boost Inverter With Inductive-Load
419 Ability," in *IEEE Transactions on Power Electronics*, vol. 34, no. 5, pp. 4014-4018, May 2019, doi:
420 10.1109/TPEL.2018.2873188.
- 421 [26] N. Sandeep and U. R. Yaragatti, "Operation and Control of an Improved Hybrid Nine-Level Inverter,"
422 in *IEEE Transactions on Industry Applications*, vol. 53, no. 6, pp. 5676-5686, Nov.-Dec. 2017, doi:
423 10.1109/TIA.2017.2737406.

- 424 [27] M. D. Siddique et al., "A Single DC Source Nine-Level Switched-Capacitor Boost Inverter Topology
425 With Reduced Switch Count," in IEEE Access, vol. 8, pp. 5840-5851, 2020, doi:
426 10.1109/ACCESS.2019.2962706.
- 427 [28] M. D. Siddique et al., "A New Single Phase Single Switched-Capacitor Based Nine-Level Boost Inverter
428 Topology With Reduced Switch Count and Voltage Stress," in IEEE Access, vol. 7, pp. 174178-174188,
429 2019, doi: 10.1109/ACCESS.2019.2957180.
- 430 [29] H. K. jahan, M. Abapour, K. Zare, S. H. Hosseini, F. Blaabjerg and Y. Yang, "A Multilevel Inverter with Minimized
431 Components Featuring Self-balancing and Boosting Capabilities for PV Applications," in IEEE Journal of Emerging
432 and Selected Topics in Power Electronics, doi: 10.1109/JESTPE.2019.2922415.



© 2020 by the authors. Submitted for possible open access publication under the terms and conditions of the Creative Commons Attribution (CC BY) license (<http://creativecommons.org/licenses/by/4.0/>).

433